Science Advances

AAAS

advances.sciencemag.org/cgi/content/full/3/5/e1602510/DC1

Supplementary Materials for

A pressure-induced topological phase with large Berry curvature in $Pb_{1-x}Sn_xTe$

Tian Liang, Satya Kushwaha, Jinwoong Kim, Quinn Gibson, Jingjing Lin, Nicholas Kioussis, Robert J. Cava, N. Phuan Ong

Published 31 May 2017, *Sci. Adv.* **3**, e1602510 (2017)
DOI: 10.1126/sciadv.1602510

This PDF file includes:

section S1. Ab initio band calculations

We have performed extensive density-functional theory calculations of the electronic structure of $Pb_{1-x}Sn_xTe$ to investigate how changes to the lattice parameter affect the states in the vicinity of the L points of the Brillouin zone (BZ) surface (this simulates application of hydrostatic pressure P). We assume the existence of a weak sublattice distortion $\mathbf{d} \parallel [111]$. At a specific pressure (identified as P_1), we find that a pair of Dirac nodes appears near each of the 3 equivalent L points. As P is raised above P_1, each Dirac node splits into a pair of Weyl nodes with opposite chirality. The Weyl nodes move in an elliptical orbit until they mutually annihilate at a higher pressure (identified as P_2). We also simulate the effect of time-reversal symmetry breaking on the Weyl pairs by introducing a finite Zeeman field. In general, the calculations agree well with the transport results reported in the main text.

The *ab initio* calculations were carried out within the framework of the projector augmented-wave formalism [23], as implemented in the Vienna *ab initio* simulation package (VASP) [24]. For the total-energy calculations, the PBEsol [25] was employed to treat the exchange-correlation potential. On the other hand, to investigate the band-gap evolution versus P, we employed the modified Becke-Johnson Local Density Approximation (MBJLDA) functional, which has been shown [26] to yield accurate band gaps, effective masses, and frontier-band ordering. Accurate determination of these parameters are especially important in the topological insulator phase. Spin-orbit coupling was included in the self-consistent calculations.

The energy cut-off of the plane-wave expansion of the basis functions was set at 300 eV and an $8\times8\times8$ k-point mesh was used in the Brillouin zone sampling. The calculated equilibrium lattice constants for SnTe and PbTe of 6.288 Å and 6.441 Å, respectively, are in good agreement with the experimental values of 6.303 Å and 6.443 Å [27].

We employ the WANNIER90 package [28] with a frozen energy window of 1 eV above the Fermi level E_F to construct Wannier functions from the outputs of the first-principles calculations for the SnTe and PbTe pristine materials. In order to determine the electronic structure of the $Pb_{1-x}Sn_xTe$ alloys we employ the virtual-crystal approximation where each Pb or Sn is replaced by a "virtual" atom whose properties are the weighted average of the two constituents. Further, for the lattice constant and the relative ferroelectric displacement x_P sampling mesh, we use a linear interpolation scheme.

Even though the MBJLDA functional gives band gap of 0.24 eV and -0.13 eV for PbTe and SnTe, respectively, in reasonable agreement with the corresponding experimental values of 0.19 eV and -0.20 eV [29], the larger calculated values lead to large values of the predicted critical pressures P_1 and P_2. Therefore, using scissor operators the on site energies of the Pb and Sn p-orbitals are adjusted to reproduce the experimental values of the band gap at the theoretical equilibrium lattice for PbTe and SnTe, namely

$$\begin{aligned} \epsilon_{\text{Pb-}p} &\longrightarrow \epsilon_{\text{Pb-}p} - 0.047 \text{ eV} \\ \epsilon_{\text{Sn-}p} &\longrightarrow \epsilon_{\text{Sn-}p} - 0.124 \text{ eV} \end{aligned} \tag{S1}$$

The response of the Weyl nodes to a magnetic field $\mathbf{B}$ is simulated by including the Zeeman energy. The direction of $\mathbf{B}$ is determined by the spinor quantization axis in the VASP calculations

$$H^{\text{Zeeman}}_{m,n}(\mathbf{k}) = \lambda\sigma_{\hat{n}} \tag{S2}$$

We investigated the two field directions $\mathbf{B} \parallel [111]$ and $\mathbf{B} \parallel [\bar{1}\bar{1}2]$. The evolution of the Weyl nodes under hydrostatic pressure and/or magnetic field is determined using a steepest descent method.

A. Emergence of Weyl phase under pressure

In the absence of the ferroelectric displacement, band inversion under pressure occurs at the four equivalent L points in $\mathbf{k}$ space. The ferroelectric atomic displacement $\mathbf{d} \parallel [111]$, which is observed in SnTe and GeTe, introduces a Rashba splitting that breaks the cubic symmetry, rendering the L_0 point (which lies in the direction [111]) inequivalent to the remaining three L points (in zero B, these equivalent points are called collectively L_1; see fig. S1). At the insulator-to-metal transition (at the lower critical pressure P_1), closing of the bulk gap at L_1 coincides with the appearance of two Dirac nodes bracketing each L_1 point. Increasing P slightly above P_1 further splits each Dirac node into a pair of Weyl nodes of opposite chirality (there are 6 Weyl pairs altogether). When the pressure exceeds P_1, the two Dirac nodes at L_1 split into four Weyl nodes, $w_1^{\pm}$ and $w_2^{\pm}$, where

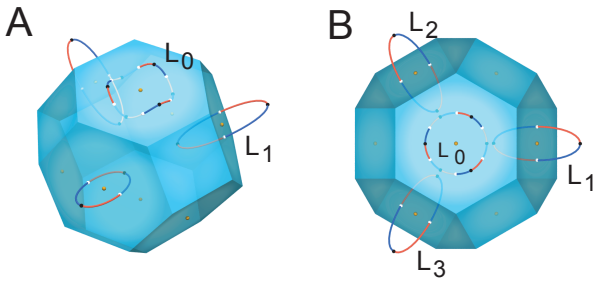

fig. S1. Calculated **k**-space trajectories of Weyl nodes in $Pb_{1-x}Sn_xTe$ ($x = 0.5$) under applied pressure in zero magnetic field. Panel (A) shows the L_0 point and the 3 equivalent L_1 points on the BZ surface in a perspective with **d** ||[111] vertical. Panel (B) shows the top-down view sighted along **d**. Trajectories of Weyl nodes with positive (negative) chirality are colored red (blue). White and black dots indicate creation and annihilation points, respectively. The orbits are shown magnified by a factor of 10 relative to the scale of the BZ.

subscripts (1, 2) identify the starting Dirac node and superscripts (+, -) refer to the chirality of the Weyl nodes. In fig. S1, the **k**-space trajectories of the nodes with +(-) chirality are colored red (blue). For clarity, the orbits displayed are magnified by a factor of 10 relative to the BZ scale. White and black dots indicate the creation and annihilation points, respectively. As noted, we have 12 Weyl nodes altogether. As P exceeds P_1, the nodes w_1^+ and w_2^- move into the interior of the first BZ, whereas w_1^- and w_2^+ move away from the interior. When P reaches the higher critical pressure P_2, the 12 Weyl nodes annihilate pair-wise simultaneously (in zero B) at the points shown as black dots. Near the L_0 point, the Weyl nodes exist over a much narrower interval of P between P_1 and P_2. The undulating trajectory of the Weyl nodes near L_0 under pressure (fig. S1) is similar to that reported in ferroelectric hexagonal BiTeI [30].

In fig. S2A, we plot the phase diagram in the plane of a vs. x_p to identify the Weyl phase in $Pb_{1-x}Sn_xTe$ ($x = 0.25$). Here, $x_p = d/d_{[111]}$ is the ferroelectric displacement d normalized to the unit-cell diagonal $d_{[111]}$. The pink wedge represents the region in which the Weyl nodes near the L_1 point are stable. As shown in the upper inset, the bulk gap at L_1 vanishes within the interval of lattice constants ($a = 6.292 \rightarrow 6.308$ Å) with x_p fixed at 0.008. The wedge separates the topological crystalline insulator phase (TCI) from the normal insulator (NI) phase. When the ferroelectric displacement vanishes ($x_p \rightarrow 0$), the rapid shrinking of the wedge implies the merging of the two Dirac cones at all the L points. This illustrates Murakami's prediction[1,2] that breaking of inversion symmetry is necessary to observe the emergence of the Weyl phase when the bulk gap is forced to close.

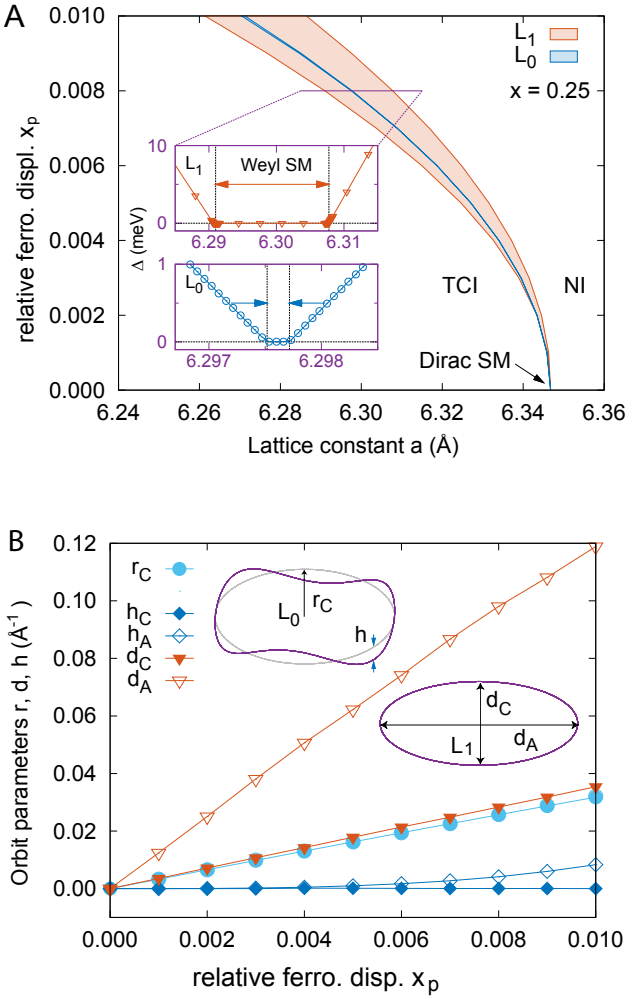

fig. S2. The phase diagram of the Weyl phase in $Pb_{1-x}Sn_xTe$ ($x = 0.25$) and orbit parameters.
Panel (A): The phase diagram of the Weyl phase in $Pb_{1-x}Sn_xTe$ ($x = 0.25$) in the plane of a vs. x_p where a is the lattice constant and x_p the relative ferroelectric displacement ($x_p \equiv d/d_{[111]}$ with $d_{[111]}$ the unit-cell diagonal along [111]). The pink wedge is where the 12 Weyl nodes near the points L_1, L_2 and L_3 are stable. The narrow blue strip indicates where the Weyl nodes exist around the L_0 point. The wedge separates the topological crystalline insulator (TCI) and normal insulator (NI) phases. The upper inset shows how the bulk gap Δ at L_1 vanishes within the lattice interval $a =$ (6.292, 6.308) Å, with x_p fixed at 0.008. The lower inset shows the bulk gap at L_0 closing within a much narrower interval of a. Panel (B) plots the increase versus x_p of r_C (the radius of the circular orbit of the Weyl nodes around L_0), and d_A and d_C (the major and minor diameters of the elliptical orbit around L_1 as sketched in the insets). Subscripts A and C refer to annihilation and creation. Also plotted is the undulation amplitude h of the orbit at L_0.

For the Sn content x =0.25, we find that Weyl nodes

appear at the L_0 point in a very narrow range of P (blue strip). Accordingly, the bulk gap at L_0 closes only over a much narrower interval (at the same x_p), as shown in the lower inset in fig. S2A.

The **k**-space orbits described by the Weyl nodes can be characterized by their radii or diameters (insets in fig. S2B). At the point L_0, the projection of the orbit onto the (111) BZ surface is circular with radius $r_C = r_A$ (subscripts C and A refer to creation and annihilation points). As shown in fig. S1A, the orbit at L_0 undulates above and below this surface with an amplitude h. By contrast, the orbits at L_1 are elliptical with major and minor diameters d_A and d_C, respectively. In the main panel of fig. S2B, we plot the monotonic increase of r_C, d_A, d_C and h_A as x_p increases. Interestingly, r_C and d_C are closely matched throughout the range of x_p explored.

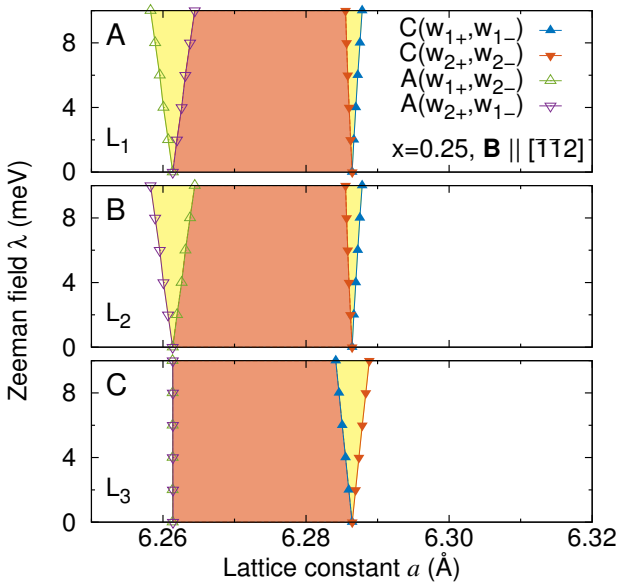

fig. S3. Phase diagram of the Weyl phase in $Pb_{1-x}Sn_xTe$ ($x = 0.25$) in the a-λ plane with applied **B** $\parallel [\bar{1}\bar{1}2]$. Breaking of the C_3 symmetry about the [111] axis by **B** makes L_3 inequivalent to L_1 and L_2 (L_3 lies in the plane spanned by **B** and [111]). $x_p = 0.01$ is used. In Panel (A), a finite Zeeman field λ splits the phase boundary for creation of Weyl nodes into two distinct boundaries (V-shaped wedge on the right). The annihilation boundaries (left) are similarly split. Panels (B) and (C) show the splitting for the nodes near L_2 and L_3, respectively. In each panel, the areas shaded orange (yellow) have four (two) Weyl nodes near each of the points L_1, L_2 and L_3.

B. Effect of Magnetic Field on the Weyl Nodes

Our calculations reveal that the Weyl node positions are highly sensitive to the time-reversal symmetry breaking effects of **B**. The effects, expressed through the Zeeman energy coupling to the spins, are senstive to the direction of **B** (in finite B, we restore the labels of L_1, L_2 and L_3).

For **B** $\parallel$ [111], one of the two Dirac nodes appears near L_1 at a critical pressure lower than in the case with $B = 0$ (correspondingly, its partner appears at a higher pressure). Hence the pair of nodes $w_1^{\pm}$ appears at a lower pressure than the pair $w_2^{\pm}$. The annihilation boudary is not affected if **B** is aligned $\parallel$[111].

By contrast, if **B** is rotated to the perpendicular direction $[\bar{1}\bar{1}2]$, the C_3 symmetry about the [111] axis is broken, which makes L_3 inequivalent to L_1 and L_2 (L_3 lies in the plane spanned by [111] and **B**). As shown in the phase diagram in fig. S3, this leads to field-induced splittings of the phase boundaries on both sides of the Weyl phase for the nodes L_1 and L_2. In fig. S3A, the phase boundary on the right (larger a) representing Weyl node creation at L_1 splits into 2 lines as λ increases. At the boundary on the left, a finite λ now also affects annihilation of the Weyl nodes. The nodes w_1^- and w_2^+ (outside the BZ volume) mutually annihilate at a pressure lower than the nodes w_1^+ and w_2^- which lie inside the BZ. As a result, the phase boundary for annihilation splits into two lines. The effects on the phase boundaries at L_2 are similar, except that the Weyl nodes are swapped on the annihilation curves. The annihilation boundary for L_3 in Panel (C) remains unsplit (annihilation of the two Weyl pairs is simultaneous).

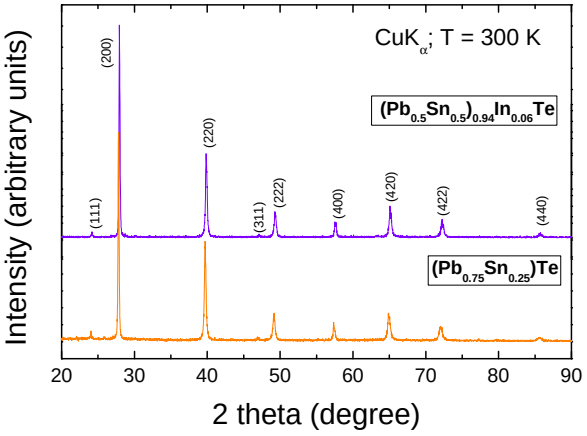

fig. S4. X-ray diffractograms of two powdered specimens of $Pb_{1-x}Sn_xTe$ taken from the crystal boules. The upper trace is for a boule with composition $(Pb_{1-x}Sn_x)_{1-y}In_yTe$, with $x = 0.5$ and $y = 0.06$). The lower trace is for a sample with composition $Pb_{1-x}Sn_xTe$ with $x = 0.25$.

To relate to the experiment, we note that fig. S3 predicts that if P is fixed either just below P_1 or just above P_2 in zero B, the sample crosses an insulator-to-metal boundary into the Weyl phase as B increases. At

5 K, this results in a very large decrease in the observed resistivity. This explains the anomalously large negative MR observed in the experiment. However, a realistic comparison with the experiment requires incorporation of the strong anisotropy of the effective g-factor [31,32]. Here we assumed an isotropic g-factor.

section S2. Field-induced anomalous hall effect

A. $Pb_{0.5}Sn_{0.5}Te$

The x-ray diffractograms recorded for two powdered specimens of two typical samples are shown in fig. S4. The grown crystals are single-phased. The diffraction peaks are in very close agreement with the rocksalt crystal structure of space group $Fm\bar{3}m$.

We focus on the topological metallic phase (regime II). As shown in Fig. 2D of the main text, the two Dirac nodes split at $P = P_1$ into two Weyl pairs at the three points L_1, L_2 and L_3. The size of the Fermi pockets grows under pressure, as evidenced by the evolution of SdH oscillations and the Hall density under pressure. As discussed in the main text, the system acquires an anomalous Hall contribution in finite B.

We first convert the measured resistivity tensor ρ_{ij} into the conductivity tensor σ_{ij} at each value of B. Additivity of the Hall conductivities gives $\sigma_{xy} = \sigma^N_{xy} + \sigma^A_{xy}$. Assuming that the normal term σ^N_{xy} is given by the conventional Drude expression, we have used the following expressions to fit the total observed Hall conductivity

$$\sigma_{xy} = \sigma^N_{xy} + \sigma^A_{xy} \tag{S3}$$

$$\sigma^A_{xy} = \sigma^0_{\rm AHE}\, g(x) \tag{S4}$$

$$g(x) = \frac{1}{[{\rm e}^{-x}+1]} \qquad x = \frac{(B-B_A)}{\Delta B} \tag{S5}$$

$$\sigma^N_{xy} = n_H e\mu\, \frac{\mu B}{1+(\mu B)^2} \tag{S6}$$

where σ^A_{xy} and σ^N_{xy} are the anomalous and Drude Hall conductivities, respectively, and n_H is the carrier density. Here, the onset of the anomalous Hall effect (AHE) around B_A was simulated numerically by a smooth step-function $g(x)$ with ΔB representing the width of the step, i.e., $x = (B - B_A)/\Delta B$.

We found that Eqs. S3 to S6 provide an excellent fit to the total (observed) σ_{xy}. To highlight the anomalous contribution, we plot in fig. S5D the measured σ_{xy} (solid curves) at the 3 pressures 16.5, 18.3 and 21.8 kbar. For comparison, we have also plotted the ordinary term σ^N_{xy} (dashed curves) given by the Drude expression Eq. S6. At each P, the difference of the 2 curves is then the anomalous term σ^A_{xy} (simulated by $f(x)$). For the curve at 21.8 kbar, σ^A_{xy} is the area shaded in pink.

An interesting feature inferred is that the AHE term fits the broadened step-function form $f(x)$ much better than say a B-linear form. The onset field B_A is close to the field at which the lowest Landau level (LL) is entered. This occurs close to the knee feature in the field profiles of ρ_{yx} (Fig. 3A of main text and fig. S5C here). Further, we note that the field profile of the effective Hall number ρ_{yx}/eB displays a pronounced increase above B_A (Fig. 2C of the main text and fig. S5B here). The results imply that the anomalous Hall response sharply increases when E_F drops into the lowest ($n = 0$) LL. This could be closely related to the chiral nature of the $n = 0$ LL, although there are no theoretical predictions specific to the Hall effect in the chiral LL.

From the fits, the strength of the AHE term $\sigma^0_{\rm AHE}$ can be determined. To show its behavior versus P, we have plotted it normalized to the hole density p as $\sigma^0_{\rm AHE}/p$ vs. P in Fig. 3C of the main text (this yields the Berry curvature averaged over the FS). The corresponding results for $Pb_{0.75}Sn_{0.25}Te$ are shown here in fig. S6B.

A finite Berry curvature leads to an anomalous velocity $\mathbf{v}_A = \mathbf{E} \times \mathbf{\Omega}(\mathbf{k})$, which engenders the anomalous Hall conductivity [33]

$$\sigma^A_{xy} = \sum_{i,\mathbf{k}} n_i(\mathbf{k})\Omega_{z,i}(\mathbf{k}) \tag{S7}$$

where the index i runs over the Weyl nodes, and n_i is the occupation number in node i. Depending on the chirality χ_i, $\mathbf{\Omega}_i(\mathbf{k})$ is directed either radially inwards or outwards. Close to the node at $\mathbf{K}_i$, the curvature has the monopole form $\mathbf{\Omega}_i(\mathbf{k}) = \chi_i \Delta\mathbf{k}_i/|\Delta\mathbf{k}_i|^3$, where $\Delta\mathbf{k}_i = \mathbf{k} - \mathbf{K}_i$ [33]. When TRS prevails (in zero B), the sum over Weyl nodes vanishes. In finite field, the Zeeman field λ shifts the Fermi energy (measured from the node) in opposite directions for different signs in χ_i. Because this directly affects $\Delta\mathbf{k}_i$, the sum in Eq. S7 yields a finite σ^A_{xy} that grows with λ.

B. $Pb_{0.75}Sn_{0.25}Te$

Next, we briefly discuss the AHE of $Pb_{0.75}Sn_{0.25}Te$. In the topological metallic phase (regime II), as shown in Panels A, C of fig. S6, the MR and Hall are essentially the same as those of $Pb_{0.5}Sn_{0.5}Te$ in regime II except that now everything is confined in a narrower range of magnetic field. Therefore, the same analyses used in previous section can be employed to yield the parameters such as anomalous Hall strength $\sigma^0_{\rm AHE}$ etc. The results are $\sigma^0_{\rm AHE} \sim 25\ \Omega^{-1}\ {\rm cm}^{-1}$ at $p = 18$ kbar. Unlike $Pb_{0.5}Sn_{0.5}Te$, in $Pb_{0.75}Sn_{0.25}Te$, high-P insulating phase (regime III) can be achieved under experimentally accessible pressure above ~ 25 kbar, signaled by the divergence of $\sigma^0_{\rm AHE}/p$ shown in Panel B of fig. S6.

The carrier density in $Pb_{0.75}Sn_{0.25}Te$ (Sample E1) at P = 21.7 kbar is 16.7 times smaller than that of $Pb_{0.5}Sn_{0.5}Te$ (Sample A2) at P = 25.4 kbar, and yet in both $Pb_{0.5}Sn_{0.5}Te$ and $Pb_{0.75}Sn_{0.25}Te$, the maximum values of the conductivities σ are nearly the same at $B = 0$

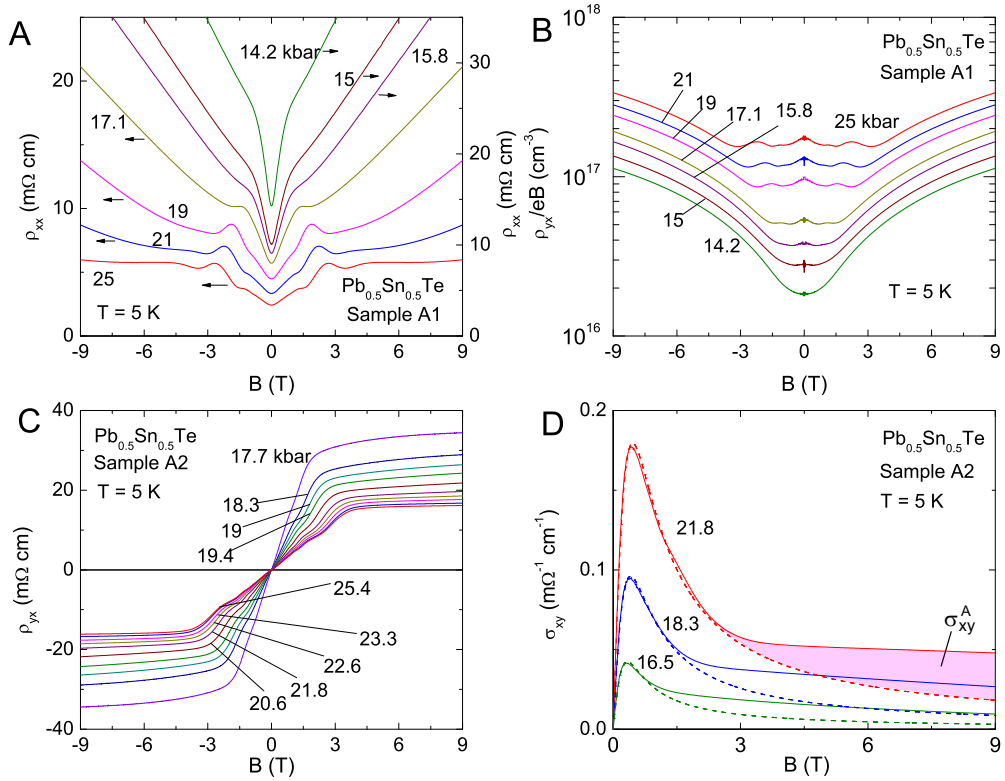

fig. S5. Supplemental data of $(Pb_{0.5}Sn_{0.5})_{1-y}In_yTe$ for samples A1 and A2.

Supplemental data of $(Pb_{0.5}Sn_{0.5})_{1-y}In_yTe$, with $y = 0.06$ taken in Samples A1 (Panels A, B) and A2 (Panels C, D). Panel (A) shows the resistivity ρ_{xx} versus a transverse B measured at 5 K and with P fixed at values 14.2 to 25 kbar for Sample A1. At each P, the oscillations below ~ 3 T correspond to SdH oscillations (the largest peak corresponds to the $n = 1$ LL). Panel (B) plots the Hall resistivity divided by Be, ρ_{yx}/Be, vs. B for Sample A1. At low fields (where SdH oscillations occur), the flat profile allows ρ_{yx}/Be to be identified with the total hole density n_H. The strong increase of ρ_{yx}/Be above 3 T reflects the onset of the AHE term. Panel (C) plots the observed curves of ρ_{yx} vs. B at 5 K for Sample A2 with P fixed at values above P_1. Instead of the conventional B-linear profile, ρ_{yx} bends over at the "knee" near 2-3 T. The unusual Hall profile suggests the appearance of an anomalous Hall conductivity that adds to the ordinary term when B exceeds the knee value. Panel (D) plots σ_{xy} vs B (derived from inverting ρ_{ij}) at 3 values of P (solid curves). By fitting to Eqs. S3-S6, we have separated the conventional Hall term σ^N_{xy} (dashed curves) from the AHE term σ^A_{xy}. The latter (shown shaded in pink for the curve at 21.8 kbar) onsets as the broadened step-function $f(x)$ at B_A.

(~ 0.7 $(m\Omega)^{-1}$ cm^{-1}). This is because the mobility for $Pb_{0.75}Sn_{0.25}Te$ ($\sim 5\pm1\times10^5$ cm^2 V^{-1} s^{-1}) is much larger than that of $Pb_{0.5}Sn_{0.5}Te$ ($\sim 2.86\times10^4$ cm^2 V^{-1} s^{-1}), allowing the system to show SdH oscillations at very low fields below ~ 1 T as shown in Panel A of fig. S6, corresponding to $k_F \sim 0.005$ Å^{-1}.

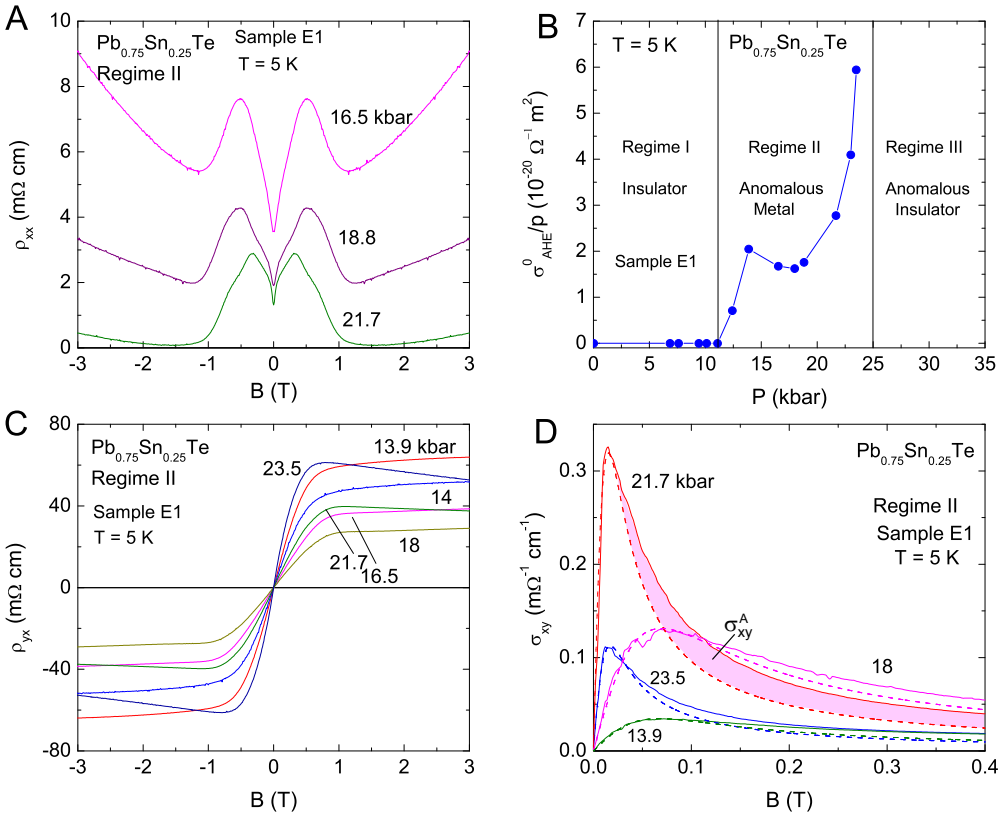

fig. S6. Supplemental data of $Pb_{0.75}Sn_{0.25}Te$ for sample E1. Panel (A) shows the resistivity ρ_{xx} versus a transverse **B** measured at 5 K, with P fixed at 16.5 kbar, 18.8 kbar, and 21.7 kbar (Regime II). At each P, the oscillations below ~ 1 T correspond to SdH oscillations (the largest peak corresponds to the n = 1 LL). Panel (B) plots the ratio of σ^A_{xy}/n_H vs. P. The ratio, proportional to $< \Omega_z >$, shows a sharp increase at $P_1 \sim 11$ kbar followed by a gentler variation in the metallic phase. As P approaches $P_2 \sim 25$ kbar, σ^A_{xy}/n_H starts to diverge, signaling the appearance of the high-P insulating phase. Panel (C) plots the observed curves of ρ_{yx} vs. B at 5 K with P fixed at values between P_1 and P_2 (Regime II). Instead of the conventional B-linear profile, ρ_{yx} bends over above ~ 1 T, suggestive of an extraordinary contribution to σ_{xy} at large B. The Hall density n_H reaches its maximum value $\sim 1.58 \times 10^{16}$ cm^{-3} at $P = 18$ kbar. Panel (D) plots σ_{xy} vs B (derived from inverting ρ_{ij}) at 4 values of P (solid curves). By fitting to Eqs. S3-S6, we have separated the conventional Hall term σ^N_{xy} (dashed curves) from the AHE term σ^A_{xy}. The latter (shown shaded in pink for the curve at 21.7 kbar) onsets as the broadened step-function $f(x)$ at B_A.